Geochemistry, Geophysics, Geosystems

RESEARCH ARTICLE
10.1029/2020GC009286

Key Points:

- A statistical analysis is introduced to study the probability of slab stagnation events in fully dynamic, self-consistent convection models
- A viscosity jump at either 660 or 1,000 km depth causes similar frequency of flat-lying slabs at ~1,000 km depth
- A viscosity jump at 1,000 km depth alone causes a lack of flat-lying slabs in the uppermost lower mantle that is inconsistent with observations

Supporting Information:

- Supporting Information S1
- Supporting Information S2
- Supporting Information S3

Correspondence to:
Y. Wang,
Email:wangym.ustc@gmail.com

Citation:
Wang, Y., & Li, M. (2020) Constraining mantle viscosity structure from a statistical analysis of slab stagnation events. *Geochemistry, Geophysics, Geosystems*, *21*, e2020GC009286. https://doi.org/10.1029/2020GC009286

Received 10 JUL 2020
Accepted 9 OCT 2020

Constraining Mantle Viscosity Structure From a Statistical Analysis of Slab Stagnation Events

Yongming Wang[1], and Mingming Li[1]

[1]School of Earth and Space Exploration, Arizona State University, Tempe, AZ, USA

Abstract The viscosity structure of Earth's mantle, even the 1-D radial viscosity profile, remains not well constrained. The dynamics of the subducting slabs is strongly affected by, and can be used to constrain, the viscosity structure of the mantle. Here, we perform fully dynamic, self-consistent mantle convection models to study the dynamics of subducted slabs in the deep mantle. We use a statistical analysis approach to quantify how the depth distribution of flat-lying slabs is affected by the depth-dependence of mantle viscosity. We find that, for cases in which the viscosity increases at 660 km depth, whether sharply or gradually, flat-lying slabs preferentially occur above this depth, and importantly, up to ~30% of the subducted slabs previously flatted at this depth later sink to the deep lower mantle and maintain a flat-lying morphology. The frequency of (or the probability to have) flat-lying slabs at ~1,000 km depth in these cases is similar to cases in which the viscosity jump occurs at 1,000 km depth. Therefore, to explain the presence of flat-lying slabs at ~1,000 km depth for the Earth does not require a viscosity jump at this depth. In contrast, a viscosity jump merely occurring at ~1,000 km depth causes a lack of flat-lying slabs in the uppermost lower mantle at ~700–900 km depth and is inconsistent with seismic observations. The presence of flat-lying slab materials in the Earth's uppermost lower mantle requires a viscosity increase at 660 km depth.

Plain Language Summary Conventionally, a stepwise mantle viscosity jump is often modeled at 660 km depth where the endothermic phase transition occurs. However, some recent studies argued that the viscosity may increase at deeper depths of ~1,000 km. Here, dynamically self-consistent mantle convection models are performed to investigate the effect of the depth-dependent mantle viscosity structure on slab morphologies. We quantify the statistics for the depth distribution of flat-lying slabs with subducted slabs freely generated as a form of thermal boundary layer instabilities in mantle convection models. The models show that a stepwise viscosity increase at ~1,000 km depth results in the absence of flat-lying slabs at intermediate depths of 700–900 km below the transition zone. This is inconsistent with seismic tomography observations which indicate significant flat-lying slab materials at ~700–900 km depths. The viscosity increase at 660 km depth is therefore essential to cause flat-lying slabs in the uppermost lower mantle.

1. Introduction

The mantle viscosity is a key factor controlling the dynamics of the Earth's interior, but even the Earth's 1-D radial viscosity profile remains under debate. It has been suggested that mantle viscosity generally increases by ~10–100 times from the upper mantle to the lower mantle, in order to explain the Earth's long-wavelength geoid anomaly (Hager & Richards, 1989; Panasyuk & Hager, 2000). Traditionally, the viscosity structure is modeled as a stepwise increase at 660 km depth where the ringwoodite to bridgmanite + ferropericlase phase transition happens (e.g., Hager & Richards, 1989; Liu & Zhong, 2016; Mitrovica & Forte, 2004). However, some geoid inversion models with many-layered viscosity structure reported an increase in viscosity around 1,000–1,200 km depth accompanied either with or without a viscosity increase at 660 km depth (e.g., Forte et al., 1991; Kido et al., 1998; King & Masters, 1992). More recent long-wavelength geoid analysis reported a viscosity increase at depths of 800–1,200 km (Rudolph et al., 2015), while studies of plume structures from seismology argued for increased mantle viscosity below ~1,000 km (French & Romanowicz, 2015). Experimental studies suggested that the viscosity in the uppermost part of the lower mantle may gradually increase down to ~1,000 km depth to reach its maximum due to potential pressure effects (Marquardt & Miyagi, 2015). The possible compositional variations of lower-mantle enrichment in

intrinsically dense basaltic lithologies may also contribute to viscosity increase at greater depths (Ballmer et al., 2015). However, results from geoid inversions on mantle viscosity structure are rather nonunique (e.g., King, 2016; Liu & Zhong, 2016; Mitrovica & Forte, 1997, 2004), and the depth for the viscosity increase in the lower mantle remains unclear with large uncertainties in geoid modeling (Richards & Lenardic, 2018).

The dynamics of the subducted slabs are greatly controlled by the viscosity of the slab and the surrounding mantle, and thus provide a pathway to constrain the mantle viscosity structure. Seismic tomography studies have revealed that while some subducting slabs directly penetrate into the lower mantle, others appear to be laterally deflected and stagnant around the base of the transition zone at a depth of ~660 km or be trapped in the uppermost lower mantle at greater depths of ~1,000 km (e.g., C. Li et al., 2008; Fukao & Obayashi, 2013; Fukao et al., 2009; Ritsema et al., 2011). According to previous geodynamic modeling experiments (e.g., Billen, 2008; Goes et al., 2017; Tackley, 1995 and references therein), the major factors that are responsible for slab stagnation include an endothermic phase transition at 660 km depth (e.g., Christensen & Yuen, 1984, 1985; Tackley et al., 1993; Torii & Yoshioka, 2007), rapid trench migration (e.g., Agrusta et al., 2017; Christensen, 1996; Torii & Yoshioka, 2007; Yoshioka & Naganoda, 2010; Zhong & Gurnis, 1995), a viscosity increase from the upper to lower mantle (e.g., Čížková & Bina, 2019; Marquardt & Miyagi, 2015; Torii & Yoshioka, 2007), slab rheology (e.g., Čížková & Bina, 2013; Čížková et al., 2002; Billen, 2008; Billen & Hirth, 2007; Garel et al., 2014), and slab buoyancy (e.g., Agrusta et al., 2014; Bina & Kawakatsu, 2010; King et al., 2015; Tetzlaff & Schmeling, 2000). The occurrence of stagnant slabs at ~1,000 km depth is interesting, which has served as a piece of evidence for viscosity jump at this depth (e.g., Fukao & Obayashi, 2013; Marquardt & Miyagi, 2015; Rudolph et al., 2015). However, Mao and Zhong (2018, 2019) recently made quantitative comparisons between 3-D global mantle convection models that used realistic plate motion history with seismic tomography models, and they found that the geodynamic models with a viscosity increase at 660 km depth plus a thin weak layer beneath the 660-km phase change boundary produce slab structures in the mantle transition zone that match tomography results equally well as models with viscosity increase at 1,000 km depth. In addition, geodynamic modeling studies by Yoshioka and Naganoda (2010) and Čížková and Bina (2019) showed that a stagnant slab at 660 km depth can eventually sink to, and maintain a flat-laying morphology in, the lower mantle, implying that a viscosity jump at 1,000 km depth may not be required to cause slab stagnation at this depth. The remaining questions are (1) what is the probability for a flatted slab at 660 km depth to maintain a flat-lying morphology after sinking into the lower mantle and (2) does a viscosity jump at 660 km depth lead to as many flat-lying slabs at ~1,000 km depth as when the viscosity jump occurs at 1,000 km?

It is worthy to note that most previous studies used either a kinematic approach in which the trench velocity and subduction velocity are imposed to the model (e.g., Čížková et al., 2002; Torii & Yoshioka, 2007; Yoshioka & Naganoda, 2010), or a partially self-consistent dynamic model in which a slab with given age, dip angle, and strength is prescribed at the subduction zone as the initial condition and the trench and subduction velocity are allowed to evolve freely with time (e.g., Agrusta et al., 2017; Čížková & Bina, 2019). These model setups are important to isolate the effects of each parameter on the dynamics of the slabs and facilitate the examination of the sensitivity of modeling results to model parameters, but it is unclear to what extent the dynamics of the prescribed subducting slab is consistent with the model's intrinsic dynamic system. In addition, previous models with imposed surface velocity mainly focused on the dynamics of a single subducting slab, which does not help answering the two questions raised at the end of the previous paragraph due to sample limit.

Here, we take a different approach to investigate how mantle viscosity structure affects the depth distribution of slab morphologies. We perform fully dynamic, self-consistent 2-D numerical simulations in which subducting slabs are naturally and continuously generated as a result of thermal boundary layer instabilities. Instead of focusing on the behavior of a single subducting slab, we introduce a statistical method to analysis the long-term stagnation events of all slabs for each model and our results place constraints on the mantle viscosity structure for the Earth.

2. Method

Numerical simulations of the slab dynamics are performed in a 2-D Cartesian geometry using the finite-element code CITCOM (Moresi & Solomatov, 1995) with modifications. The conservation equations of the mass, momentum, and energy are solved for an incompressible fluid under the Boussinesq approximation:

Table 1
Model Parameters

Parameters	Values
Model depth, D_0	2,800 km
Model width, L_0	8,400 km
Reference mantle density, ρ_0	3,300 kg/m^3
Gravitational acceleration, g	9.8 m/s^2
Reference thermal expansivity, α_0	3×10^{-5}/K
Temperature difference, ΔT	2500 K
Reference thermal diffusivity, κ_0	10^{-6} m^2/s
Gas constant, R_{gas}	8.31 J/(K mol)
Specific heat, C_p	1,250 J/(kg K)
Phase change density change, $\Delta\rho$	300 kg/m^3
Phase change width, δ	35 km
Phase change reference temperature, T_0	1573 K
Phase change reference depth, d_0	660 km

$$\nabla \cdot \vec{u} = 0 \tag{1}$$

$$-\nabla P + \nabla \cdot \left(\eta \dot{\varepsilon}\right) = \left(RaT - Ra^{p}\Gamma\right)\hat{z} \tag{2}$$

$$\frac{\partial T}{\partial t} + \left(\vec{u} \cdot \nabla\right)T = \nabla^2 T + H \tag{3}$$

where $\vec{u}$, P, η, $\dot{\varepsilon}$, Ra, T, $\hat{z}$, t, and H are velocity, dynamic pressure, viscosity, strain rate, thermal Rayleigh number, temperature, unit vector in vertical direction, time, and internal heating rate, respectively. Ra^p and Γ are Rayleigh number and phase function for the phase change, respectively. The equations are nondimensionalized by introducing the following characteristic scales (primed variables are dimensional):

$$x_i = x_i' / D_0$$

$$u_i = u_i' D_0 / \kappa_0$$

$$T = T' / \Delta T$$

$$t = t' \kappa_0 / D_0^2$$

$$P = \frac{P' D_0^2}{\eta_0 \kappa_0} \tag{4}$$

where D_0, κ_0, ΔT, and η_0 are model thickness, reference diffusivity, temperature difference between bottom and surface, and reference viscosity, respectively. The thermal and phase-change Rayleigh number are defined as:

$$Ra = \frac{\alpha_0 \rho_0 g \Delta T D_0^3}{\kappa_0 \eta_0} \tag{5}$$

$$Ra^{p} = \frac{\Delta\rho g D_0^3}{\kappa_0 \eta_0} \tag{6}$$

where α_0 and ρ_0 in Equation 5 are reference thermal expansivity and reference mantle density, respectively. $\Delta\rho$ in Equation 6 is the density contrast of the phase change. g is the gravitational acceleration. Reference values of physical parameters used for nondimensionalization are provided in Table 1. In most of our models we use a Rayleigh number of $Ra = 5 \times 10^7$, but we also explored the effects of other values of Ra from 2×10^7 to 2×10^8.

A phase-change function formulation is used to simulate the phase transition (Christensen & Yuen, 1985; M. M. Li et al., 2018; Zhong & Gurnis, 1994). Γ is defined in dimensionless form as:

$$\Gamma = \frac{1}{2}\left[1 + \tanh\left(\frac{\pi}{\delta}\right)\right] \tag{7}$$

where δ is the phase change width and π is the dimensionless "excess pressure" as:

$$\pi = d - d_0 - \gamma\left(T - T_0\right) \tag{8}$$

where d is the depth, d_0 and T_0 are the reference depth and temperature of the phase change, and γ is the Clapeyron slope. Recent high *P-T* mineral physics experiments have reported that the Clapeyron slope for the endothermic phase transition is about −0.4 to −2.5 MPa/K (e.g., Fei et al., 2004; Katsura et al., 2003;

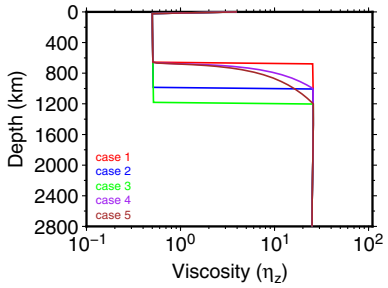

Figure 1. Depth-dependent viscosity profiles used in this study. Case 1 (red) has a sharp viscosity increase at 660 km depth. Case 2 (blue) has a sharp viscosity increase at 1,000 km depth. Case 3 (green) has a sharp viscosity increase at 1,200 km depth. Case 4 (purple) has a smooth viscosity increase from 660 to 1,000 km depth, and case 5 (suntan) has a smooth viscosity increase from 660 to 1,200 km depth.

Litasov et al., 2005), which is much smaller than previous measurement of −3.0 MPa/K (e.g., Ito & Takahashi, 1989). Mao and Zhong (2018) also found that a too large Clapeyron slope (~3.0 MPa/K) would produce unrealistic slab stagnation in the southern Pacific that is not observed seismically. Therefore, most of our models use a moderate $\gamma = -2.0$ MPa/K which is within the recent reported range, but we also explored the effects of other values of γ from 0 to −3.0 MPa/K. The physical parameters related to the phase transition are listed in Table 1. We will show in the next section that the exothermic phase transition at 410 km depth and the latent heating due to phase transition have little effects on our results, and for simplicity, they are not considered in our models if not specifically pointed out.

We use a depth- and temperature-dependent viscosity, with $\eta(T,z) = \eta_z \exp\left[E\left(0.5 - T\right)\right]$, where $E = 6.91$ (~144 kJ/mol), normalized by $R_{gas}\Delta T$ with R_{gas} being the gas constant (Table 1), is the dimensionless activation energy which results in a viscosity varying by 3 orders of magnitude for a temperature ranging from 0 to 1. We use this relatively small activation energy to allow for sufficient deformation of the boundary layer in generating subducting slabs since we do not consider dislocation creep and other deformation mechanisms (i.e., yield stress) in our models. η_z is a viscosity pre-factor which is 1.0 in the upper mantle and is varied case by case in the deep mantle. We tested different structures of η_z including (1) a stepwise viscosity increase at 660 km, (2) a stepwise viscosity increase at 1,000 or 1,200 km, and (3) a smooth viscosity increase from 660 to 1,000 km or 1,200 km (Figure 1). In most of our models, the viscosity increases by a factor of 50, but we also tested other values of 10, 30, or 100 in some models for comparison.

The model domain extends from the surface to 2,800 km depth and the horizontal extent is 8,400 km. It is divided uniformly into 768 and 256 elements in the horizontal and vertical direction, respectively, leading to a grid resolution of ~10 km in both directions.

The surface temperature is prescribed as a constant of nondimensional $T = 0$ (0°C), whereas the bottom is thermally insulating to prohibit the formation of upwelling plumes as the size and effect of plumes in our 2-D Cartesian models would be overestimated. The models are internally heated with a nondimensional heating rate of $H = 20$ to avoid fast cooling of the numerical models. The velocity boundary conditions for top and bottom boundaries are free-slip. The side walls are periodic for both the temperature and velocity boundary conditions. The initial temperature is $T = 0.6$ throughout the model domain imposed by small perturbations with a magnitude of 10^{-2}. All models have been run for a long enough time (at least 4 Ga) and we focus on examining the results when the convection models are in a statistical-steady state, that is the effect of initial condition has been taken over by the intrinsic dynamics of the system.

In our models, the surface cools with time following a half-space cooling law that leads to thickening of the top boundary layer and subducting slabs are generated as a form of boundary layer instabilities. We focus on understanding how and how frequent the subducting slabs become flat-lying at different depths. We adopt the following approach to identify flat-lying slabs in numerical models. For a given time step, at each depth, we determine the minimum temperature T_{min}, the horizontally averaged temperature T_{ave} and the background temperature T_{bg} which is the average temperature for regions with $T < T_{ave}$. The cold downwelling materials are then defined as regions where the temperature satisfies $T < T_{bg} - f(T_{bg} - T_{min})$, where $f = 0.01$ sets the threshold for subducted slabs. Note that this approach of defining slabs is similar to previous studies to define mantle plumes (e.g., Leng & Zhong, 2008; Zhong, 2006). If the horizontal length scale of a continuous slab segment is larger than 500 km, we define it as a flat-lying slab at this depth, that is, a stagnation event is determined. The stagnation time for a stagnation event of the flat-lying slab is determined as the time interval between the current and next time step.

While the increased viscosity in the lower mantle is supposed to thicken the subducting slabs by approximately twice (Gaherty & Hager, 1994; Gurnis & Hager, 1988), slab buckling is able to cause even larger thickening to 400–800 km (e.g., Behounkova & Cizkova, 2008; Lee & King, 2011; Ribe et al., 2007) to be

consistent with that from seismic observations (e.g., Kárason & Van Der Hilst, 2000). In addition, the length scale of the horizontally deflected slab is generally 500–1,500 km from seismic observations (Goes et al., 2017 and references therein). Therefore, we choose a criterion of 500 km in our numerical models to quantify a flat-lying slab by which we are able to account for both the horizontal deflection and buckling of the slabs, and to exclude slab thickening solely due to the thermal diffusion. We also examined the effects of other criteria of 750 and 1,000 km on our model results as will be shown later.

We quantify the total time of the stagnation events in the depth range of 300–1,500 km with a bin size of 10 km and within a time window from 200 Ma to 4,000 Ma. We choose this time window to (1) avoid the effect of initial condition and (2) allow a large enough time window for statistical analysis. We measure the total amount of stagnation time at each depth bin within the time window and normalize it with the size of the time window (i.e., 3,800 Myr). We also considered the situation when multiple flat-lying slabs occur at the same depth for a given time snapshot and we summed up the amount of stagnation time for all flat-lying slabs. It is therefore expected that the total stagnation time at each depth measured by the above approach maybe sometimes even larger than the size of the time window. For convenience, we define the normalized time as the flat-slab frequency. We also tried a different approach in which we measured the flat-slab frequency for each depth by summing up the time when at least one flat-lying slab is identified at this depth (e.g., without adding up the stagnation time for multiple slabs), but the result remains nearly the same as we will show later.

3. Results

In this section, we first examine how different types of depth-dependent mantle viscosity as shown in Figure 1 affect the behaviors of subducting slabs in the deep mantle. We then examine the influences of other parameters on the results, including the Clapeyron slope, the magnitude of the viscosity increase, and the Rayleigh number which represents the vigor of convection (see Table 2 for all models).

3.1. The Effects of Viscosity Structure

We first show the results of case 1 which uses a 50-times stepwise viscosity jump at 660-km depth, a Clapeyron slope of $\gamma = -2.0$ MPa/K for the 660-km phase transition and a Rayleigh number of $Ra = 5 \times 10^7$. Figure 2 shows several snapshots of the temperature field for this case, illustrating three types of subducted slab behaviors. The first type of slabs directly penetrate to the lower mantle without being horizontally deflected or buckled (e.g., Figure 2a). The second type of slabs are horizontally deflected when they approach the 660-km phase change boundary, causing slab lying laterally at the base of the transition zone (e.g., Figure 2b). The third type of slabs accumulate and spread out laterally when they reach the 660-km boundary, leading to slab buckling and flat-lying slabs around this boundary (e.g., Figure 2c). Eventually, the third type of slabs pass through the 660-km boundary and sink into the lower mantle which is similar to a "slab avalanche" event (e.g., Movie S1), with many of them still maintaining a flat-lying shape (e.g., Figure 2d).

The variable slab behaviors shown in Figure 2 are largely controlled by trench migration. For the slab shown in Figure 2b which is horizontally deflected at the base of the transition zone, the slab root at the surface has traveled ~700 km within 60 Myr, corresponding to an average trench migration rate of ~1.15 cm/yr (Figures 3a–3d). This is consistent with previous studies which suggested that a trench velocity of 1.0 cm/yr is able to cause slab stagnation (e.g., Stegman et al., 2010; Torii & Yoshioka, 2007). This trench velocity is also comparable to that observed from the Earth, which shows a mean trench retreat rate of 0.6–1.1 ± 3.0 cm/yr (Lallemand & Heuret, 2017; Lallemand et al., 2008). While for the slab shown in Figure 2c with accumulative buckling, the slab root moves ~100 km within 100 Myr, corresponding to an average trench migration rate of only ~0.1 cm/yr (Figures 3e–3h). These results indicate that in the presence of rapid trench migration, subducting slabs are typically deflected horizontally above the transition zone; however, without rapid trench migration, subducting slabs either directly penetrate the 660-km boundary (Figure 2a) or are accumulatively buckled above the boundary (Figure 2c). A similar relationship between trench velocities and slab behaviors has also been documented in previous studies, which suggested that horizontally deflected slabs exhibit moderate trench retreat (e.g., 0.5–1.5 cm/yr) while vertical sinking slabs always accompanied with a quasistationary trench (e.g., Agrusta et al., 2017; Garel et al., 2014; Stegman et al., 2010). We also find that, without rapid trench migration,

Table 2
Model Input Parameters[a]

Model	η_{depth}(km)	η_z	γ (MPa/K)	*Ra*	η_{type}
Case 1	660	50	−2	5×10^7	Sharp
Case 2	1,000	50	−2	5×10^7	Sharp
Case 3	1,200	50	−2	5×10^7	Sharp
Case 4	1,000	50	−2	5×10^7	Smooth
Case 5	1,200	50	−2	5×10^7	Smooth
Case 1-1	660	50	0	5×10^7	Sharp
Case 1-2	660	50	−1	5×10^7	Sharp
Case 1-3	660	50	−3	5×10^7	Sharp
Case 1-4	660	10	−2	5×10^7	Sharp
Case 1-5	660	30	−2	5×10^7	Sharp
Case 1-6	660	100	−2	5×10^7	Sharp
Case 1-7	660	50	−2	2×10^7	Sharp
Case 1-8	660	50	−2	1×10^8	Sharp
Case 1-9	660	50	−2	2×10^8	Sharp
Case 2-1	1,000	50	0	5×10^7	Sharp
Case 2-2	1,000	50	−1	5×10^7	Sharp
Case 2-3	1,000	50	−3	5×10^7	Sharp
Case 2-4	1,000	10	−2	5×10^7	Sharp
Case 2-5	1,000	30	−2	5×10^7	Sharp
Case 2-6	1,000	100	−2	5×10^7	Sharp
Case 2-7	1,000	50	−2	2×10^7	Sharp
Case 2-8	1,000	50	−2	1×10^8	Sharp
Case 2-9	1,000	50	−2	2×10^8	Sharp
Case 3-1	1,200	50	0	5×10^7	Sharp
Case 3-2	1,200	50	−1	5×10^7	Sharp
Case 3-3	1,200	50	−3	5×10^7	Sharp
Case 3-4	1,200	10	−2	5×10^7	Sharp
Case 3-5	1,200	30	−2	5×10^7	Sharp
Case 3-6	1,200	100	−2	5×10^7	Sharp
Case 3-7	1,200	50	−2	2×10^7	Sharp
Case 3-8	1,200	50	−2	1×10^8	Sharp
Case 3-9	1,200	50	−2	2×10^8	Sharp
Case 4-1	1,000	50	0	5×10^7	Smooth
Case 4-2	1,000	50	−1	5×10^7	Smooth
Case 4-3	1,000	50	−3	5×10^7	Smooth
Case 4-4	1,000	10	−2	5×10^7	Smooth
Case 4-5	1,000	30	−2	5×10^7	Smooth
Case 4-6	1,000	100	−2	5×10^7	Smooth
Case 4-7	1,000	50	−2	2×10^7	Smooth
Case 4-8	1,000	50	−2	1×10^8	Smooth
Case 4-9	1,000	50	−2	2×10^8	Smooth
Case 5-1	1,200	50	0	5×10^7	Smooth

Table 2
Continued

Model	η_{depth}(km)	η_z	γ (MPa/K)	*Ra*	η_{type}
Case 5-2	1,200	50	−1	5×10^7	Smooth
Case 5-3	1,200	50	−3	5×10^7	Smooth
Case 5-4	1,200	10	−2	5×10^7	Smooth
Case 5-5	1,200	30	−2	5×10^7	Smooth
Case 5-6	1,200	100	−2	5×10^7	Smooth
Case 5-7	1,200	50	−2	2×10^7	Smooth
Case 5-8	1,200	50	−2	1×10^8	Smooth
Case 5-9	1,200	50	−2	2×10^8	Smooth
Case 1-0[b]	660	50	−2	5×10^7	Sharp
Case 2-0[b]	1,000	50	−2	5×10^7	Sharp
Case 3-0[b]	1,200	50	−2	5×10^7	Sharp
Case 4-0[b]	1,000	50	−2	5×10^7	Smooth
Case 5-0[b]	1,200	50	−2	5×10^7	Smooth

[a] η_{depth} is the viscosity increase depth in the lower mantle, η_z is the magnitude of the increased viscosity in the lower mantle, γ is the Clapeyron slope at 660-km phase transition, *Ra* is the input Rayleigh number, η_{type} indicates whether the viscosity increases sharply at η_{depth} (sharp) or linearly increases from 660 km depth to η_{depth} (smooth).
[b]These are additional cases with respect to cases 1-5 by considering the 410-km phase transition and the latent heating due to phase change (both 410 and 670 km) under the extended Boussinesq approximation.

the slab that directly penetrates to the lower mantle (Figure 2a) is colder and thicker than the slab that first accumulates at 660-km depth before sinking to the lower mantle (Figures 2c and 2d).

The morphology of the subducting slabs changes with time and the flat-lying of the slabs is a temporary phenomenon (e.g., Movie S1). We therefore quantify the frequency of stagnation events for all flat-lying slabs at each depth in the deep mantle. We define all slabs whose lateral extent is larger than 500 km as flat-lying slabs (Section 2), no matter what mechanism causes this large extent. As shown in Figure 4a, flat-lying slabs for case 1 preferentially occur above the 660-km discontinuity, for example, the flat-slab frequency at ~600 km depth is up to ~70% (Figure 4a), meaning that for most (near ~70%) of the model run time, there is at least one flat-lying slab at this depth. This is mainly due to the coexistence of the phase transition and the viscosity jump at the 660-km discontinuity, both of which facilitate the lateral deflection of the subducted slabs. Note that the highest occurrence of flat-lying slabs does not occur exactly at 660 km depth but slightly above it because of the thickness of the slabs. The sinking of the slabs from the base of the transition zone to the lower mantle leads to some slabs with wide lateral extension in the lower mantle (e.g., Figures 2c and 2d). The flat-slab frequency is ~20%–30% at depths deeper than 660 km (Figure 4a), meaning about one third of the previous flat-lying slabs above the 660-km depth eventually sink to the deep lower mantle and also maintain a flat-lying morphology.

Case 2 has similar parameters as case 1, except that the viscosity jump now occurs at 1,000 km depth (Figure 1). Like case 1, we also observe three types of slab behaviors as shown in Figure 5. Some slabs directly penetrate the phase transition zone and sink into the lower mantle accompanied by slab thickening (e.g., Figure 5a), some slabs are laterally deflected at the base of the transition zone (Figure 5b), and some slabs buckle and spread laterally above the 1,000-km depth where the viscosity jump is present (Figure 5c) and they later sink to deeper depths while still maintaining a wide lateral-extent morphology (Figure 5d). Interestingly, we do not observe slab buckling at 660 km depth for case 2, which indicates that the endothermic phase transition alone is not able to cause slab accumulation at this depth. We find that the average trench velocity for the horizontally deflected slab in Figure 5b is ~1.25 cm/yr (Figures S3a–S3d, slab root moves ~900 km

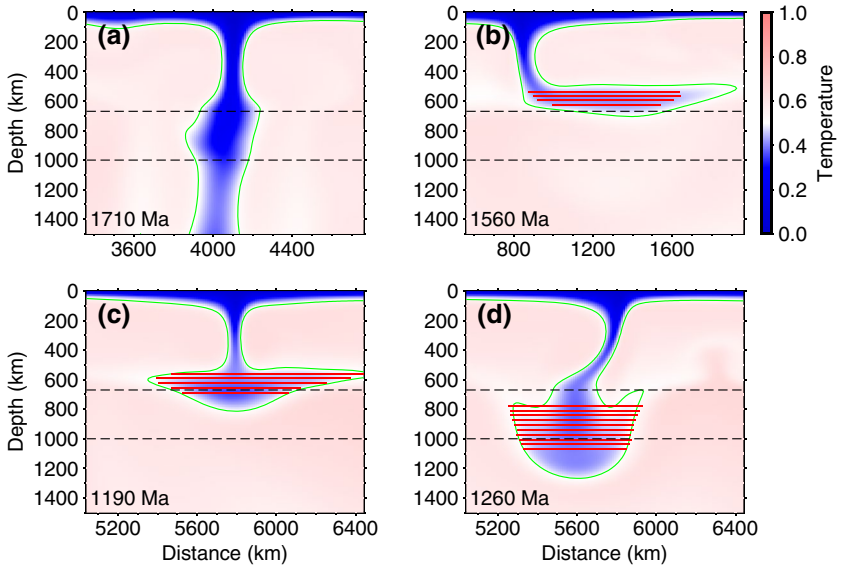

Figure 2. Snapshots of the temperature field showing different morphologies of subducted slabs for case 1, which has a Clapeyron slope of $\gamma = -2.0$ MPa/K, a Rayleigh number of $Ra = 5 \times 10^7$ and a stepwise viscosity increase of $\eta_z = 50$ at 660 km depth. (a) A slab vertically penetrates to the lower mantle. (b) A slab is horizontally deflected at 660 km depth. (c) A slab first accumulates at 660 km depth (d) and then sinks to the lower mantle while maintaining a flat-lying morphology. The two dashed lines in each panel correspond to the depths of 660 and 1,000 km, respectively. The green lines in each panel are the contours of temperature $T = 0.5$ which show the main body of the subducting slabs. The red lines in (b–d) denote the identified flat-lying slabs at different depths. Note that the ends of the red lines showing regions of flat-lying slabs, which are used for further statistical analysis, may not necessarily match the boundaries of the green contours due to different definition of the two. Only a part of the model domain is shown in each panel and the full temperature field for each panel is provided in Figure S1. A full-time evolution for case 1 is provided in Movie S1.

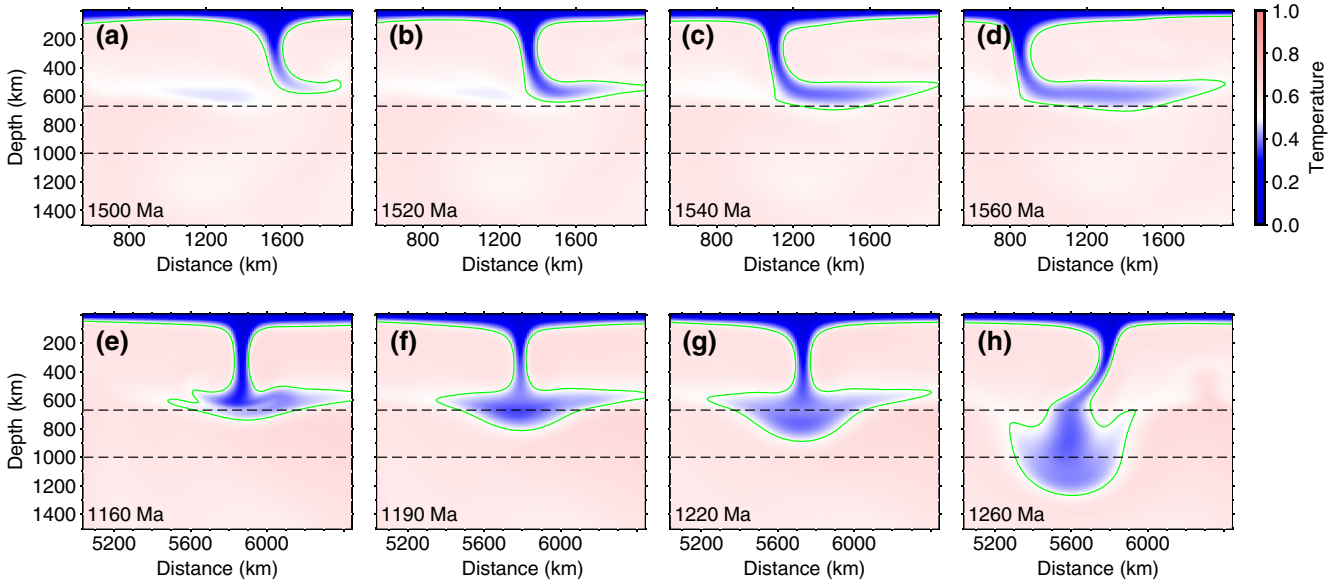

Figure 3. Snapshots of the temperature field showing the time evolution for different types of slab behaviors for case 1, which has a Clapeyron slope of $\gamma = -2.0$ MPa/K, a Rayleigh number of $Ra = 5 \times 10^7$ and a stepwise viscosity increase of $\eta_z = 50$ at 660 km depth. (a–d) The evolution of the same slab as shown in Figure 2b, for which the slab is horizontally deflected due to rapid trench migration. (e–h) The evolution of the same slab as shown in Figures 2c and 2d, for which substantial slab buckling occurs with minor trench migration.

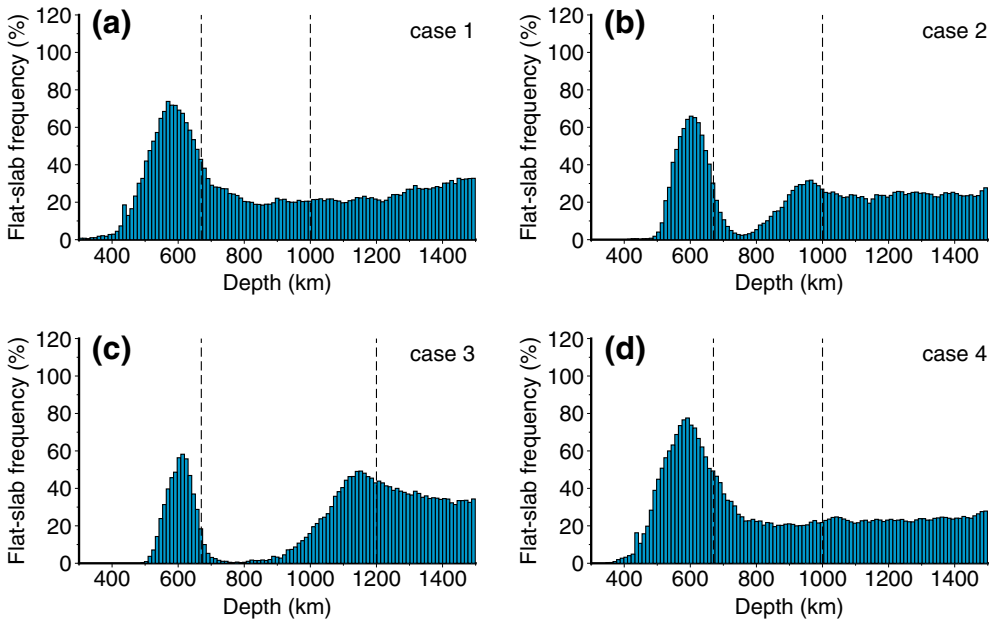

Figure 4. The frequency of flat-lying slabs as a function of depth for case 1 (a), case 2 (b), case 3 (c), and case 4 (d). Case 1 has a stepwise viscosity increase at 660 km depth. Case 2 has a stepwise viscosity increase at 1,000 km depth. Case 3 has a stepwise viscosity increase at 1,200 km depth. Case 4 has a smooth viscosity increase from 660 to 1,000 km depth. All cases have endothermic phase transition at 660-km depth with a Clapeyron slope of $\gamma = -2.0$ MPa/K, a Rayleigh number of $Ra = 5 \times 10^7$ and a viscosity pre-factor of $\eta_z = 50$ for the lower mantle. The vertical dashed lines show the depths of 660, 1,000 and 1,200 km, respectively.

over 40 Myr). While for the buckled slab in Figures 5c and 5d, the average trench migration rate is about 0.44 cm/yr (Figures S3e–S3h, slab root migrates ~150 km over 34 Myr). This is consistent with our previous discussion for case 1 that the horizontal deflection of the subducting slabs is caused by rapid trench migration, while the accumulative buckling of the slabs occurs without rapid trench migration.

The statistics of the depth distribution of flat-slab frequency for case 2 is shown in Figure 4b. Similar to case 1 (Figure 4a), there is a peak of flat-slab frequency (up to ~65%) at depths just above the 660-km discontinuity (Figure 4b). Interestingly, there is a lack of flat-lying slabs at a depth range of ~660–850 km (Figure 4b). This is because a subducted slab is either horizontally deflected and trapped at the 660-km boundary in the case of rapid trench migration (e.g., Figure 5b), or sinks nearly vertically to the lower mantle when there is no rapid trench migration (e.g., Figures 5a and 5c). Many slabs become flat-lying above the 1,000-km depth due to the viscosity jump at this depth, which are characterized by accumulation and laterally spread out of slab materials (e.g., Figures 5c and 5d). The flat-lying slabs above 660 km depth are typically driven by rapid trench migration without much accumulation or buckling, which easily warm up and are difficult to sink into the lower mantle, while flat-lying slabs at 1,000 km depth due to accumulative buckling could continue sinking to greater depths by maintaining a buckling morphology. The flat-slab frequency at ~660 km depth for case 2 is ~30%, which is much smaller than case 1 with ~45% (Figure 4) due to the lack of slab accumulation at 660 km depth for case 2. The flat-slab frequency at ~1,000 km depth for case 2 is ~30%, which is comparable to case 1 of ~25% at the same depth, suggesting that a viscosity jump at either 660 km depth or 1,000 km depth leads to a similar amount of flat-lying slabs at ~1,000 km depth.

Case 3 uses the same parameters as case 2, except that the viscosity jump now is present at 1,200 km depth (Figure 1). The slab behaviors in case 3 are quite similar to case 2, which are characterized by vertical penetration, horizontal deflection, and accumulative buckling, except that the accumulation of the subducting slabs now occurs from 1,200 km depth (e.g., Figure S4). As shown in Figure 4c, two peaks of flat-slab frequency occur at depths just above 660 km where there is endothermic phase transition and around 1,200 km where the viscosity jump is present. There is also a gap in the uppermost lower mantle that lacks flat-lying slabs and this gap is much wider than that in case 2 due to the deeper viscosity jump depth.

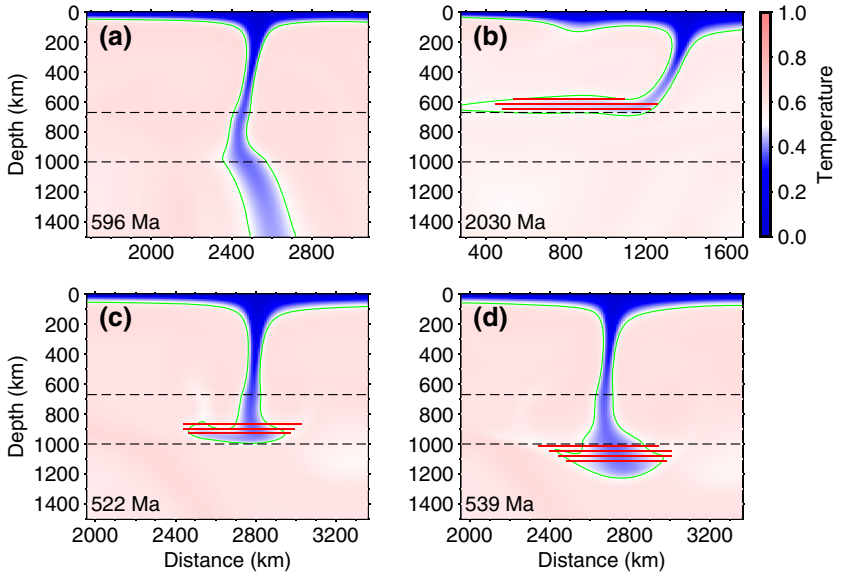

Figure 5. Snapshots of the temperature field showing different morphologies of subducted slabs for case 2, which has a Clapeyron slope of $\gamma = -2.0$ MPa/K, a Rayleigh number of $Ra = 5 \times 10^7$, and a stepwise viscosity increase of $\eta_z = 50$ at 1,000 km depth. (a) A slab vertically penetrates to the lower mantle. (b) A slab is horizontally deflected at 660 km depth. (c) A slab first accumulates at 1,000 km depth (d) and then sinks to the lower mantle while maintaining a flat-lying morphology. The two dashed lines in each panel correspond to the depths of 660 and 1,000 km, respectively. The green lines in each panel are the contours of temperature $T = 0.5$ which show the main body of the subducting slabs. The red lines in (b–d) denote the identified flat-lying slabs at different depths. Note that the ends of the red lines showing regions of stagnant slabs, which are used for further statistical analysis, may not necessarily match the boundaries of the green contours due to different definition of the two. Only a part of the model domain is shown in each panel and the full temperature field for each panel is provided in Figure S2. A full time evolution for case 2 is provided in Movie S2.

In cases 4 and 5, the viscosity pre-factor η_z increases smoothly from $\eta_z = 1$ at 660 km depth to $\eta_z = 50$ at 1,000 and 1,200 km depth, respectively (Figure 1). In both cases, the flat-lying slabs are characterized by either horizontal deflection or accumulative buckling near the 660-km depth, and some of the flat-lying slabs retain their buckling morphology when they sink to greater depths. The depth distribution of the flat-slab frequency for cases 4 and 5 (Figures 4d and S6) are nearly the same as that for case 1 (Figure 4a). It has to be pointed out that the overall pattern of the flat-slab frequency that is calculated by excluding the effects of multiple flat-lying slabs (Section 2) shows no significant difference for each reference case when compared to Figure 4, although the amplitude of the frequency at some depths is reduced (Figure S7). In addition, we examine the effect of using different criteria in defining the flat-lying slabs, that is, the threshold of flat-lying slab width is 750 or 1,000 km instead of 500 km. As shown in Figure S8a, the pattern of the depth distribution of the flat-slab frequency for a slab width of 750 km is similar to that for a slab width of 500 km, except that the magnitude of the frequency has reduced. When the threshold of the flat-lying slab width is 1,000 km, flat-lying slabs are rare in the deep mantle below the 660-km depth (Figure S8b). It has to be pointed out that the relatively long flat-lying slabs of >1,000 km are also only seismically observed above the 660-km depth (Fukao & Obayashi, 2013; Goes et al., 2017). Therefore, a threshold width of 500 or 750 km in our models is more reasonable to account for flat-lying slabs at all depths than a width of 1,000 km. We also perform cases in which the exothermic phase transition at 410 km depth and the latent heating due to phase changes (both at 410 and 660 km depth) are both considered under the extended Boussinesq approximation. We find their effects on the depth-distribution of flat-lying slabs are rather minor (Figure S9).

3.2. The Effects of Clapeyron Slope

In the above reference cases 1-5, we use a regular Clapeyron slope of $\gamma = -2.0$ MPa/K for the 660-km phase transition. We now examine the effects of Clapeyron slope by varying γ to 0 MPa/K (cases 1-1, 2-1, 3-1, 4-1, and 5-1), −1.0 MPa/K (cases 1-2, 2-2, 3-2, 4-2, and 5-2), and −3.0 MPa/K (cases 1-3, 2-3, 3-3, 4-3, and 5-3).

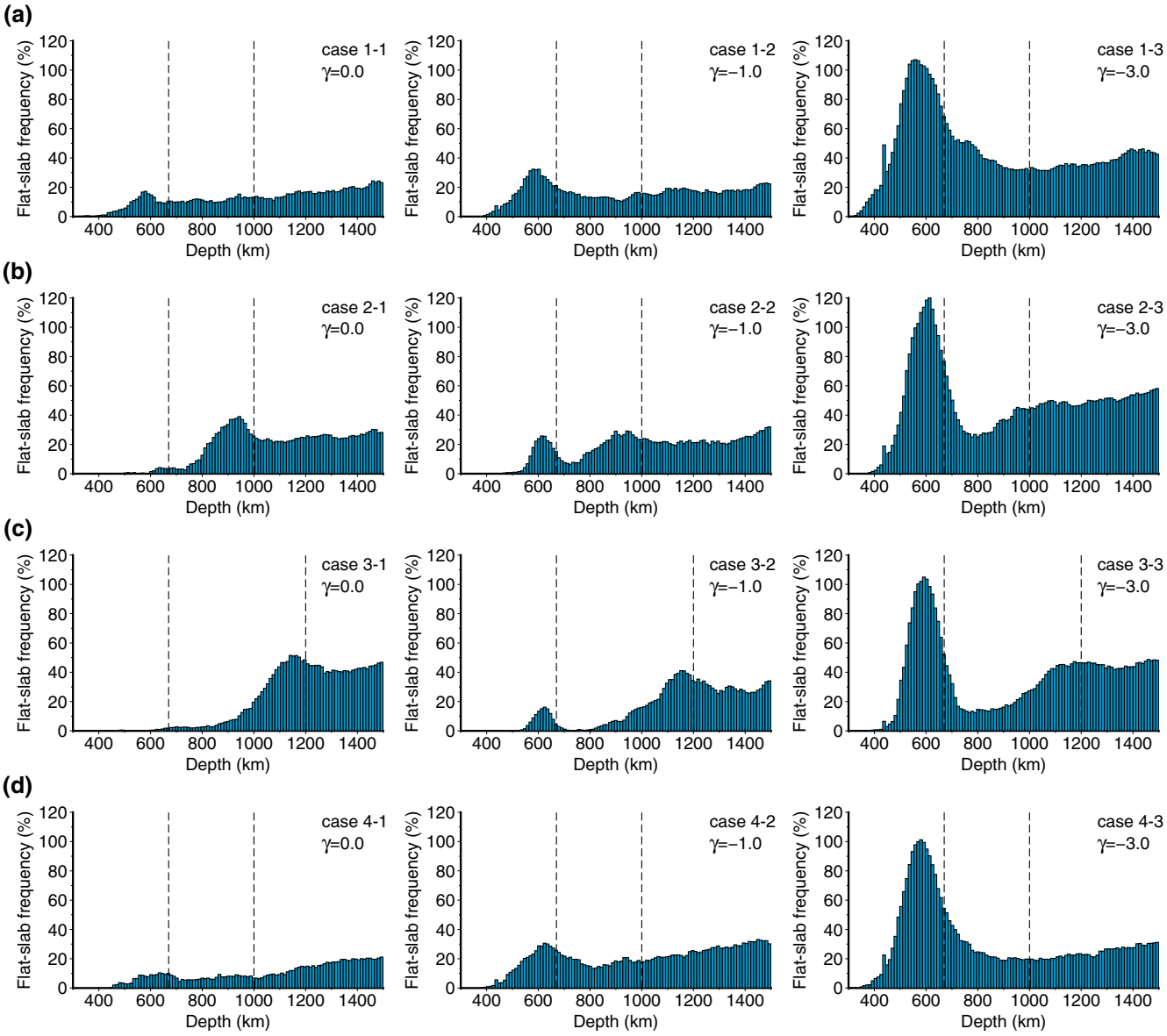

Figure 6. The frequency of flat-lying slabs as a function of depth for cases with different Clapeyron slopes, based on the reference cases of case 1 (a), case 2 (b), case 3 (c), and case 4 (d).

The statistics of the flat-slab frequency for these new cases are shown in Figures 6 and S10. Generally, with a given viscosity structure, a larger magnitude of Clapeyron slope for the 660-km phase transition leads to more flat-lying slabs around this depth and at greater depths below the transition zone (Figures 4, 6, and S10). Interestingly, when there is a viscosity increase at 660 km depth (no matter whether it is a sharp or smooth increase), flat-lying slabs can still occur around the 660-km discontinuity even though the Clapeyron slope is reduced to 0 MPa/K (Figures 6a, 6d, and S10). In such cases, the increased viscosity alone can provide sufficient resistances in hindering the subducted slabs, and the stagnation events are caused by both horizontal deflection and accumulative buckling of the slabs (e.g., Figure 2). However, when the depth of the sharp viscosity increase is moved to 1,000–1,200 km, slabs can only become flat-lying above the 660-km depth when the negative Clapeyron slope for the phase transition at this depth is larger than −1.0 MPa/K (Figures 6b and 6c), and just above ~1,000–1,200 km depth, and there remains a depth range of ~700–900 km that lacks flat-lying slabs unless the magnitude of the Clapeyron slope reaches −3.0 MPa/K (Figures 6b and 6c). With a Clapeyron slope of −3.0 MPa/K, many slab accumulation events occur at 660-km depth

even though there is no viscosity jump at this depth, and the accumulated slabs later sink to the lower mantle and many of them maintain a flat-lying morphology.

3.3. The Effects of the Magnitude of Viscosity Increase

In the reference cases 1-5, the magnitude of the increased viscosity from the upper to lower mantle, i.e., the viscosity pre-factor η_z, is set to 50X. In this section, we show the effects of different η_z of 10X (cases 1-4, 2-4, 3-4, 4-4, and 5-4), 30X (cases 1-5, 2-5, 3-5, 4-5, and 5-5), and 100X (cases 1-6, 2-6, 3-6, 4-6, and 5-6). For a given viscosity structure as shown in Figure 1, a larger η_z leads to more flat-lying slabs around the depth with viscosity increase, that is, for cases 1-(4, 5, 6), cases 4-(4, 5, 6), and cases 5-(4, 5, 6) at 660 km depth, for cases 2-(4, 5, 6) at 1,000 km depth, and for cases 3-(4, 5, 6) at 1,200 km depth, respectively (Figures 4, 7, and S11). This is because with a larger magnitude of the increased viscosity in the lower mantle, the subducted slabs are more easily accumulated above the viscosity increase boundary, since it is more difficult for slabs to directly penetrate the boundary. The enhanced accumulation of subducted slabs therefore results in more flat-lying slabs at the viscosity increase depth and also depths below due to the subsequent sinking of the slabs (Figures 4 and 7). However, the variation of the viscosity pre-factor does not significantly affect the absence of flat-lying slabs (i.e., the gap) in the uppermost lower mantle for cases in which the viscosity jump occurs at 1,000–1,200 km depth (Figures 7b and 7c). With a relatively small viscosity jump of $\eta_z = 10X$, the flat-lying slabs mostly occur around the 660-km discontinuity, and flat-lying slabs rarely occur at depths below 660 km, even when the viscosity increase occurs at 660 km depth (Figures 7a, 7d, and S11). In contrast, even when there is no viscosity increase at 660 km depth, a higher viscosity at greater depths of 1,000–1,200 km promotes slabs to be flatted at 660 km depth (Figures 7b and 7c). This is consistent with previous studies which suggested that a high-viscosity zone below 1,200 km depth could act as a resistive force to facilitate slab stagnation around a depth of 660 km (Yoshioka & Naganoda, 2010).

3.4. The Effects of Rayleigh Number

In the reference cases 1-5, the Rayleigh number is 5×10^7. In this section, we show the results of models with a different Rayleigh number of 2×10^7 (cases 1-7, 2-7, 3-7, 4-7, and 5-7), 1×10^8 (cases 1-8, 2-8, 3-8, 4-8, and 5-8) and 2×10^8 (cases 1-9, 2-9, 3-9, 4-9, and 5-9). For a given viscosity structure, a larger Rayleigh number leads to a less stable convection pattern and often a larger trench migration rate which leads to a higher probability of the subducted slabs to be horizontally deflected. In addition, a larger Rayleigh number also leads to a relatively thinner thermal boundary layer or a thinner slab which promotes flat-lying slabs as well. Therefore, a larger Rayleigh number results in more flat-lying slabs around 660 km depth (Figures 4, 8, and S12). However, the variation of the Rayleigh number does not significantly affect the depth distribution of flat-lying slabs below the 660 km depth (Figures 4, 8, and S12). In particular, for cases with viscosity jump at 1,000–1,200 km depth, the gap in the uppermost lower mantle with a lack of flat-lying slabs still exists, even when the flat-lying slabs have been significantly enhanced around the 660-km depth (Figures 8b and 8c). This further demonstrates what we have discussed in Section 3.1, that is, the flat-lying slabs characterized by horizontal deflection caused by rapid trench migration do not substantially sink to greater depths in the lower mantle, and the flat-lying slabs at greater depths below the transition zone are dominated by accumulative buckling of the subducted slabs.

4. Discussion

In this study, we perform fully dynamic and self-consistent numerical modeling experiments to study the dynamics of subducting slabs in the deep mantle. Our models have a free-slip surface boundary condition, and subducting slabs form naturally as a result of thermal boundary layer instability. We examine the behaviors of all subducting slabs in the deep mantle during a ~4,000 Myr time-window of the model run. Due to the intrinsic unstable nature of the convection system, we observe a large variation of slab morphologies from time to time (Movies S1 and S2). We therefore argue that, for our models, a statistical analysis of the behaviors of all subducting slabs is more robust than focusing on the dynamics of a single slab. Our models also include the endothermic phase transition at 660 km depth, and we test the effects of different structures of the increased viscosity from the upper to lower mantle. The rheology employed in our models did not

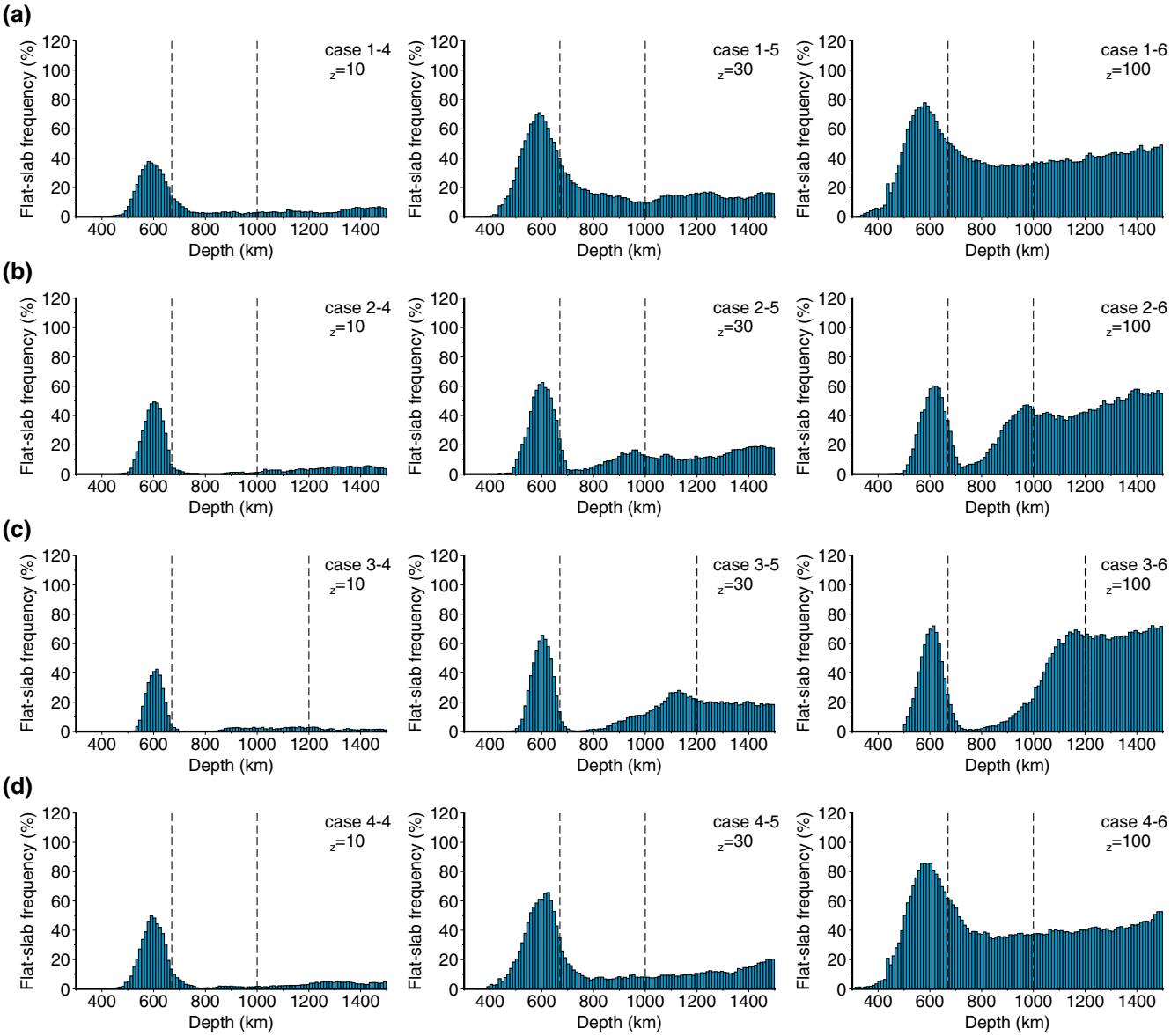

Figure 7. The frequency of flat-lying slabs as a function of depth for cases with different magnitudes of viscosity increase, based on the reference cases of case 1 (a), case 2 (b), case 3 (c), and case 4 (d).

consider the dislocation creep or other deformation mechanisms (e.g., yielding process) which may affect the slab strength and trench velocity as suggested by previous studies. However, the large population of slabs that we examined already cover a wide range of slab strengths, and our models already have a wide range of trench migration rates because the convection pattern often varies from time to time and model to model. In addition, we here focus on the influence of the depth-dependence of viscosity structure. It is not our goal here to examine the influence of other factors (e.g., water and other deformation mechanisms), some of which are not well constrained such as the amount of water in the mantle and its influences on mantle viscosity.

Importantly but not surprisingly, our numerical modeling experiments that employ fully dynamic models and use statistical analysis confirm some of the previous geodynamic modeling results. We confirm that the trench migration rate significantly affects whether the subducting slabs can penetrate the discontinuities with phase transition and/or viscosity jump, which is relatively well known (e.g., Christensen, 1996;

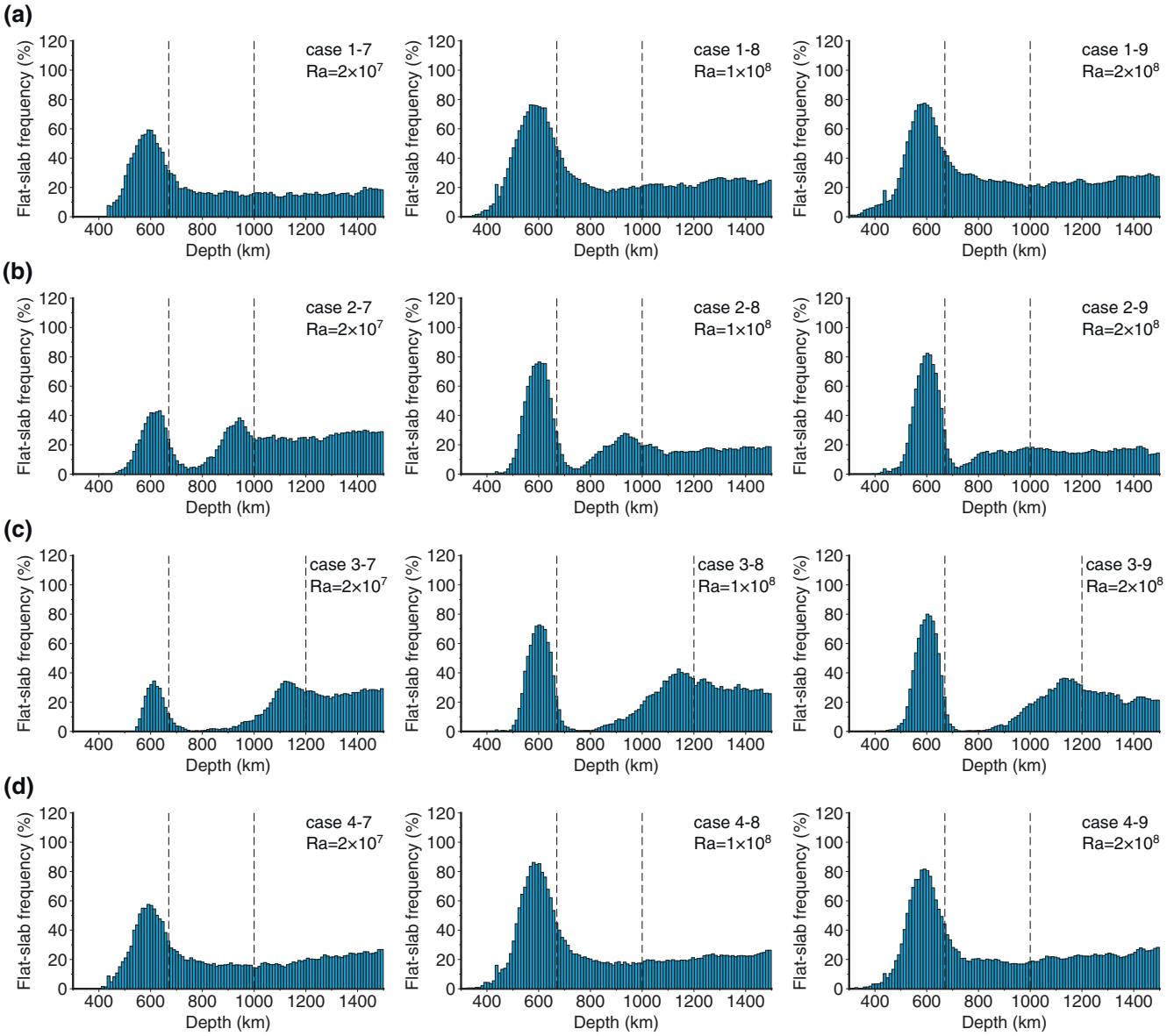

Figure 8. The frequency of flat-lying slabs as a function of depth for cases with different Rayleigh numbers, based on the reference cases of case 1 (a), case 2 (b), case 3 (c), and case 4 (d).

Čížková et al., 2002; Torii & Yoshioka, 2007). With rapid trench migration, subducting slabs are always horizontally deflected and lay above the discontinuities. In such a situation, the flat-lying slabs often become warm and weak due to thermal diffusion and are difficult to penetrate the discontinuities. Without a rapid trench migration, the subducting slabs tend to directly penetrate the discontinuities. We also find that when a subducting slab is relatively warm and weak, it is more likely to first accumulate into large volume and wide lateral extent above the discontinuities before sinking through the discontinuities, therefore, this accumulative buckling of the subducting slabs can also result in significant flat-lying slabs (e.g., >500 km) that are temporally stagnant (e.g., Figures 2 and 5).

We show that the viscosity structure of the deep mantle plays an important role in controlling the occurrence of flat-lying slabs in the uppermost lower mantle. We find that if there is a sharp viscosity jump at 660 km depth, flat-lying slabs mostly occur above this depth, but significant flat-lying slabs also occur at greater depths below the transition zone in the deep mantle. However, if the sharp increase of viscosity occurs at 1,000–1,200 km depth, then flat-lying slabs mostly occur at 660 km depth and 1,000–1,200 km depth. These

results are expected and consistent with previous studies (e.g., Ballmer et al., 2015; Čížková & Bina, 2019; Yoshioka & Naganoda, 2010). We find that a smooth increase of viscosity from 660 to 1,000–1,200 km depth has similar effects to a sharp viscosity increase on the depth distribution of flat-lying slabs, as also shown recently by Čížková and Bina (2019). We also find that a viscosity increase at 1,000–1,200 km depth promotes slab lying at 660 km depth as well, similar to that found by Yoshioka and Naganoda (2010).

One important new finding from using our statistical analysis is that there is a lack of flat-lying slabs in the uppermost lower mantle when the viscosity increase occurs at 1,000–1,200 km depth. This is because in such case, the subducting slabs either become flat-lying and are trapped above the 660-km depth in the presence of rapid trench migration, or directly sink to the lower mantle and some become flat-lying near 1,000–1,200 km depth. The resistance due to phase transition at 660 km depth alone, with a regular Clapeyron slope of −2.0 MPa/K, is not sufficient to cause subducting slabs to first accumulate into large volume and lateral extent before sinking to the lower mantle. In addition, we find that when the viscosity increases at 660 km depth, a significant amount (up to about one third) of the flat-lying slabs above 660 km depth later sinks to the lower mantle and maintains a flat-lying morphology. Importantly, the frequency of flat-lying slabs at ~1,000 km depth is similar between cases with a viscosity jump at either 660 or 1,000 km depth. A viscosity jump at ~1,000 km depth is not required to cause flat-lying slabs at this depth.

Finally, we discuss how our results can help understand the mantle viscosity structure. Seismic tomography observations have shown that although most of the stagnant slabs are found at depths of ~660 km, there are also many subducting slabs being deflected and trapped in the uppermost lower mantle (e.g., Fukao & Obayashi, 2013; van der Meer et al., 2018). Figures 9a–9c show three vertical cross-sections of the tomography model (GAP_P4, Fukao and Obayashi [2013]) with clearly flat-lying slabs that occur at a range of depths from the base of the transition zone to ~1,000 km. Another piece of evidence implying that significant slab materials have been trapped at all depths from the transition zone to depths ~1,000 km is shown in Figures 9d–9f, in which we quantify how much percentage of the global area at each depth in the mantle is occupied by subducted slabs with higher-than-average seismic velocities from both *P*-wave and *S*-wave tomography models. We find that in all three *P*-wave models and the *S*-wave model of SP12RTS, there is a local peak of the areal

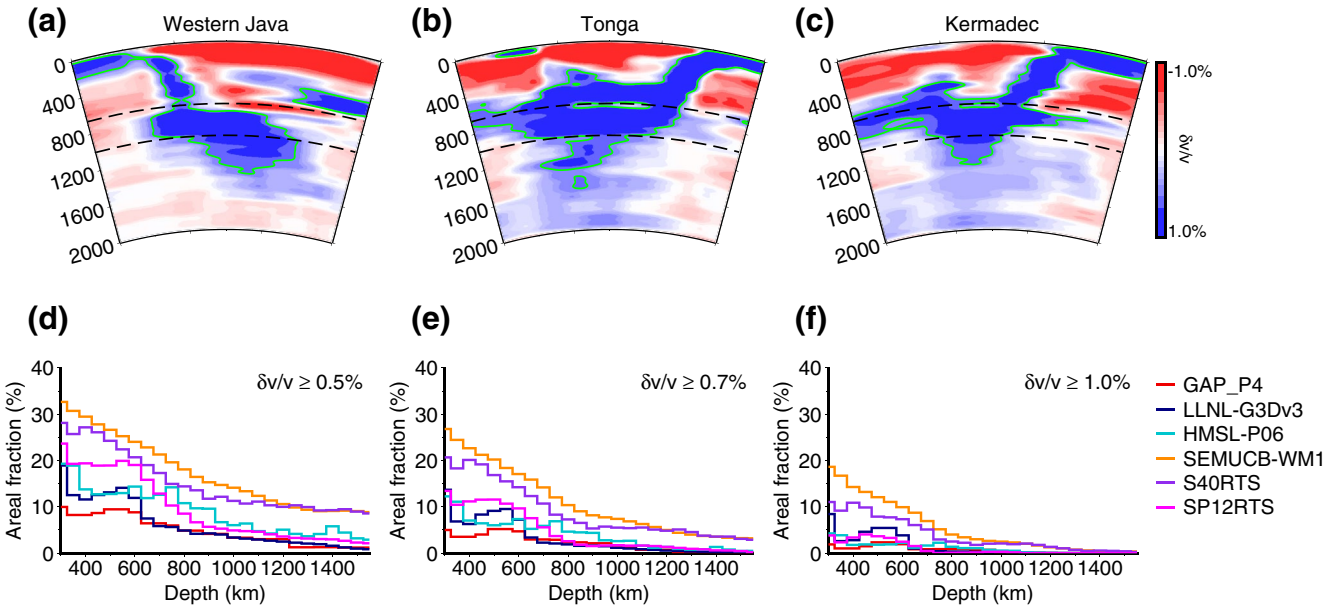

Figure 9. (a–c) Vertical cross-sections of slab images at Western Java, Tonga, and Kermadec from seismic tomography model GAP_P4 (Fukao & Obayashi, 2013). The detailed locations of the cross-sections can be found in Fukao and Obayashi (2013). In (a–c), the dashed lines denote the 660 and 1,000 km depth, respectively, and the green lines are contours of positive velocity anomaly of 0.5%. (d–f) The percentages of global area that is occupied by subducted slabs with positive seismic velocity anomalies as a function of depth. The seismic tomography models include three *P*-wave models GAP_P4 (Fukao & Obayashi, 2013), LLNL-G3Dv3 (Simmons et al., 2012), HMSL-P06 (Houser et al., 2008), and three *S*-wave models SEMUCB-WM1 (French & Romanowicz, 2014), S40RTS (Ritsema et al., 2011), and SP12RTS (Koelemeijer et al., 2015). We tested three different thresholds of the seismic velocities to identify subducted slabs, including 0.5%, 0.7%, and 1.0% for both *Vp* and *Vs* anomalies.

percentage at ~600 km depth, and for model HMSL-P06 (green curve), a local peak is also observed at ~800 km depth which has a similar value to that at 600 km depth. The areal percentage in models of EMUCB-WM1 and S40RTS decreases monotonically with the increase of depth to ~800–900 km. There is no significant depth variation of areal percentage below 1,000 km depth for all model regardless of the velocity threshold chosen to define slab materials. Nevertheless, the areal percentage of slab materials at ~660–900 km depths is always higher than that for depths > 1000 km, which is consistent with Figures 9a–9c, showing that flat-lying slabs exist in the uppermost lower mantle. We emphasize that here we do not intend to make a one-to-one comparison between our models and seismic observations, but to make the point that seismic observations show significant flat-lying slabs in the uppermost lower mantle, which (based on our modeling results) requires a viscosity increase at 660 km depth and cannot be caused by a viscosity jump merely at ~1,000–1,200 km depth.

5. Conclusions

In this study, using a series of 2-D self-consistent, fully dynamic mantle convection models, we investigate what is the mechanism that causes, and the statistic depth-distribution of, flat-lying slabs in the deep mantle. The systematic study shows that the flat-lying slab is caused by two end-member mechanisms: One is characterized by horizontal deflection of the subducting slabs in the presence of rapid trench migration, and the other by accumulative buckling of slab materials in the case of no rapid trench migration. Both the phase change buoyancy due to a negative Clapeyron slope and the viscosity increase can trigger horizontally deflected type of flat-lying slabs if rapid trench migration exists. However, the viscosity increase is crucial for flat-lying slabs caused by accumulative buckling of the subducted slabs.

We find that, if the viscosity increases at 660 km depth, no matter whether it is sharp or smooth, significant flat-lying slabs occur above this depth. In such a case, many of the flat-lying slabs with sufficient accumulation eventually sink to the lower mantle and maintain their flat-lying morphology from 660 km depth to greater depths of ~1,000 km. A viscosity jump at 660 km depth causes a similar frequency of flat-lying slabs at ~1,000 km depth when the same viscosity jump occurs at ~1,000 km. Therefore, a viscosity increase at ~1,000–1,200 km depth is not required to explain the observed flat-lying slabs at ~1,000–1,200 km depth. In contrast, although a viscosity increase at ~1,000–1,200 km depth alone helps subducted slabs to become flat-lying at 660 km depth, it leads to a lack of flat-lying slabs at ~700–900 km depths which is inconsistent with the presence of flat-lying slabs in the uppermost lower mantle observed for the real Earth.

Data Availability Statement

The numerical code and other data that support the findings of this study are available from the corresponding author upon reasonable request.

Acknowledgments
We thank three anonymous reviewers and Editor Thorsten Becker for their insightful and constructive reviews and comments that significantly improve the paper. The work is supported by NSF grant EAR-1849949 and EAR-1855624. The geodynamic models were performed on the Agave supercomputer at Arizona State University. Figures are drawn using the Generic Mapping Tools (GMT, www.soest.hawaii.edu/gmt/). The seismic tomography models are available at the websites http://d-earth.jamstec.go.jp/GAP_P4/(GAP_P4), http://ds.iris.edu/spud/earthmodel (LLNL-G3Dv3 and HMSL-P06), http://seismo.berkeley.edu/wiki_br/Main_Page (SEMUCB-WM1) and https://jritsema.earth.lsa.umich.edu (S40RTS and SP12RTS), respectively.

References

Agrusta, R., Goes, S., & van Hunen, J. (2017). Subducting-slab transition-zone interaction: Stagnation, penetration and mode switches. *Earth and Planetary Science Letters*, *464*, 10–23. https://doi.org/10.1016/j.epsl.2017.02.005

Agrusta, R., van Hunen, J., & Goes, S. (2014). The effect of metastable pyroxene on the slab dynamics. *Geophysical Research Letters*, *41*(24), 8800–8808. https://doi.org/10.1002/2014gl062159

Ballmer, M. D., Schmerr, N. C., Nakagawa, T., & Ritsema, J. (2015). Compositional mantle layering revealed by slab stagnation at similar to 1000-km depth. *Science Advances*, *1*(11), 1–9. https://doi.org/10.1126/sciadv.1500815

Behounkova, M., & Cizkova, H. (2008). Long-wavelength character of subducted slabs in the lower mantle. *Earth and Planetary Science Letters*, *275*(1–2), 43–53. https://doi.org/10.1016/j.epsl.2008.07.059

Billen, M. I. (2008). Modeling the dynamics of subducting slabs. *Annual Review of Earth and Planetary Sciences*, *36*, 325–356. https://doi.org/10.1146/annurev.earth.36.031207.124129

Billen, M. I., & Hirth, G. (2007). Rheologic controls on slab dynamics. *Geochemistry, Geophysics, Geosystems*, *8*(Q08012), 1–24. https://doi.org/10.1029/2007gc001597

Bina, C. R., & Kawakatsu, H. (2010). Buoyancy, bending, and seismic visibility in deep slab stagnation. *Physics of the Earth and Planetary Interiors*, *183*(1–2), 330–340. https://doi.org/10.1016/j.pepi.2010.04.010

Christensen, U. R. (1996). The influence of trench migration on slab penetration into the lower mantle. *Earth and Planetary Science Letters*, *140*(1–4), 27–39. https://doi.org/10.1016/0012-821x(96)00023-4

Christensen, U. R., & Yuen, D. A. (1984). The interaction of a subducting lithospheric slab with a chemical or phase-boundary. *Journal of Geophysical Research*, *89*(Nb6), 4389–4402. https://doi.org/10.1029/JB089iB06p04389

Christensen, U. R., & Yuen, D. A. (1985). Layered convection induced by phase-transitions. *Journal of Geophysical Research*, *90*(Nb12), 291–300. https://doi.org/10.1029/JB090iB12p10291

Čížková, H., & Bina, C. R. (2013). Effects of mantle and subduction-interface rheologies on slab stagnation and trench rollback. *Earth and Planetary Science Letters*, *379*, 95–103. https://doi.org/10.1016/j.epsl.2013.08.011

Čížková, H., & Bina, C. R. (2019). Linked influences on slab stagnation: Interplay between lower mantle viscosity structure, phase transitions, and plate coupling. *Earth and Planetary Science Letters*, *509*, 88–99. https://doi.org/10.1016/j.epsl.2018.12.027

Čížková, H., van Hunen, J., van den Berg, A. P., & Vlaar, N. J. (2002). The influence of rheological weakening and yield stress on the interaction of slabs with the 670 km discontinuity. *Earth and Planetary Science Letters*, *199*(3–4), 447–457. https://doi.org/10.1016/S0012-821X(02)00586-1

Fei, Y., Van Orman, J., Li, J., van Westrenen, W., Sanloup, C., Minarik, W., et al. (2004). Experimentally determined postspinel transformation boundary in Mg_2SiO_4 using MgO as an internal pressure standard and its geophysical implications. *Journal of Geophysical Research*, *109*(B02305), 1–8. https://doi.org/10.1029/2003jb002562

Forte, A. M., Peltier, W. R., & Dziewonski, A. M. (1991). Inferences of mantle viscosity from tectonic plate velocities. *Geophysical Research Letters*, *18*(9), 1747–1750. https://doi.org/10.1029/91gl01726

French, S. W., & Romanowicz, B. A. (2014). Whole-mantle radially anisotropic shear velocity structure from spectral-element waveform tomography. *Geophysical Journal International*, *199*(3), 1303–1327. https://doi.org/10.1093/gji/ggu334

French, S. W., & Romanowicz, B. (2015). Broad plumes rooted at the base of the Earth's mantle beneath major hotspots. *Nature*, *525*(7567), 95–99. https://doi.org/10.1038/nature14876

Fukao, Y., & Obayashi, M. (2013). Subducted slabs stagnant above, penetrating through, and trapped below the 660 km discontinuity. *Journal of Geophysical Research-Solid Earth*, *118*(11), 5920–5938. https://doi.org/10.1002/2013jb010466

Fukao, Y., Obayashi, M., Nakakuki, T., & Grp, D. S. P. (2009). Stagnant slab: A review. *Annual Review of Earth and Planetary Sciences*, *37*, 19–46. https://doi.org/10.1146/annurev.earth.36.031207.124224

Gaherty, J. B., & Hager, B. H. (1994). Compositional vs. thermal buoyancy and the evolution of subducted lithosphere. *Geophysical Research Letters*, *21*(2), 141–144. https://doi.org/10.1029/93GL03466

Garel, F., Goes, S., Davies, D. R., Davies, J. H., Kramer, S. C., & Wilson, C. R. (2014). Interaction of subducted slabs with the mantle transition-zone: A regime diagram from 2-D thermo-mechanical models with a mobile trench and an overriding plate. *Geochemistry, Geophysics, Geosystems*, *15*(5), 1739–1765. https://doi.org/10.1002/2014gc005257

Goes, S., Agrusta, R., van Hunen, J., & Garel, F. (2017). Subduction-transition zone interaction: A review. *Geosphere*, *13*(3), 644–664. https://doi.org/10.1130/Ges01476.1

Gurnis, M., & Hager, B. H. (1988). Controls of the structure of subducted slabs. *Nature*, *335*(6188), 317–321. https://doi.org/10.1038/335317a0

Hager, B. H., & Richards, M. A. (1989). Long-wavelength variations in earths geoid - physical models and dynamical implications. *Philosophical Transactions of the Royal Society A-Mathematical Physical and Engineering Sciences*, *328*(1599), 309–327. https://doi.org/10.1098/rsta.1989.0038

Houser, C., Masters, G., Shearer, P., & Laske, G. (2008). Shear and compressional velocity models of the mantle from cluster analysis of long-period waveforms. *Geophysical Journal International*, *174*(1), 195–212. https://doi.org/10.1111/j.1365-246X.2008.03763.x

Ito, E., & Takahashi, E. (1989). Postspinel transformations in the system Mg_2SiO_4-Fe_2SiO_4 and some geophysical implications. *Journal of Geophysical Research*, *94*(B8), 10637–10646. https://doi.org/10.1029/JB094iB08p10637

Kárason, H., & Van Der Hilst, R. D. (2000). Constraints on mantle convection from seismic tomography & *The History and Dynamics of Global Plate Motions*, *121*, 277–288). https://doi.org/10.1029/GM121p0277

Katsura, T., Yamada, H., Shinmei, T., Kubo, A., Ono, S., Kanzaki, M., et al. (2003). Post-spinel transition in Mg_2SiO_4 determined by high P-T in situ X-ray diffractometry. *Physics of the Earth and Planetary Interiors*, *136*(1–2), 11–24. https://doi.org/10.1016/S0031-9201(03)00019-0

Kido, M., Yuen, D. A., Cadek, O., & Nakakuki, T. (1998). Mantle viscosity derived by genetic algorithm using oceanic geoid and seismic tomography for whole-mantle versus blocked-flow situations. *Physics of the Earth and Planetary Interiors*, *107*(4), 307–326. https://doi.org/10.1016/S0031-9201(98)00077-6

King, S. D. (2016). An evolving view of transition zone and midmantle viscosity. *Geochemistry, Geophysics, Geosystems*, *17*(3), 1234–1237. https://doi.org/10.1002/2016gc006279

King, S. D., Frost, D. J., & Rubie, D. C. (2015). Why cold slabs stagnate in the transition zone. *Geology*, *43*(3), 231–234. https://doi.org/10.1130/G36320.1

King, S. D., & Masters, G. (1992). An inversion for radial viscosity structure using seismic tomography. *Geophysical Research Letters*, *19*(15), 1551–1554. https://doi.org/10.1029/92gl01700

Koelemeijer, P., Ritsema, J., Deuss, A., & van Heijst, H.-J. (2015). SP12RTS: A degree-12 model of shear- and compressional-wave velocity for Earth's mantle. *Geophysical Journal International*, *204*(2), 1024–1039. https://doi.org/10.1093/gji/ggv481

Lallemand, S., & Heuret, A. (2017). *Subduction zones parameters, reference module in Earth systems and environmental sciences*, London, UK: Elsevier.

Lallemand, S., Heuret, A., Faccenna, C., & Funiciello, F. (2008). Subduction dynamics as revealed by trench migration. *Tectonics*, *27*(TC3014), 1–15. https://doi.org/10.1029/2007TC002212

Lee, C., & King, S. D. (2011). Dynamic buckling of subducting slabs reconciles geological and geophysical observations. *Earth and Planetary Science Letters*, *312*(3–4), 360–370. https://doi.org/10.1016/j.epsl.2011.10.033

Leng, W., & Zhong, S. J. (2008). Controls on plume heat flux and plume excess temperature. *Journal of Geophysical Research*, *113*(B04408), 1–15. https://doi.org/10.1029/2007jb005155

Litasov, K., Ohtani, E., Sano, A., Suzuki, A., & Funakoshi, K. (2005). In situ X-ray diffraction study of post-spinel transformation in a peridotite mantle: Implication for the 660-km discontinuity. *Earth and Planetary Science Letters*, *238*(3–4), 311–328. https://doi.org/10.1016/j.epsl.2005.08.001

Liu, X., & Zhong, S. J. (2016). Constraining mantle viscosity structure for a thermochemical mantle using the geoid observation. *Geochemistry, Geophysics, Geosystems*, *17*(3), 895–913. https://doi.org/10.1002/2015gc006161

Li, C., van der Hilst, R. D., Engdahl, E. R., & Burdick, S. (2008). A new global model for P wave speed variations in Earth's mantle. *Geochemistry, Geophysics, Geosystems*, *9*(Q05018), 1–21. https://doi.org/10.1029/2007gc001806

Li, M. M., Zhong, S. J., & Olson, P. (2018). Linking lowermost mantle structure, core-mantle boundary heat flux and mantle plume formation. *Physics of the Earth and Planetary Interiors*, *277*, 10–29. https://doi.org/10.1016/j.pepi.2018.01.010

Mao, W., & Zhong, S. J. (2018). Slab stagnation due to a reduced viscosity layer beneath the mantle transition zone. *Nature Geoscience*, *11*(11), 876–881. https://doi.org/10.1038/s41561-018-0225-2

Mao W., Zhong S. (2019). Controls on global mantle convective structures and their comparison with seismic models. *Journal of Geophysical Research: Solid Earth*, *124*, (8), 9345–9372. https://doi.org/10.1029/2019jb017918.

Marquardt, H., & Miyagi, L. (2015). Slab stagnation in the shallow lower mantle linked to an increase in mantle viscosity. *Nature Geoscience*, *8*(4), 311–314. https://doi.org/10.1038/Ngeo2393

Mitrovica, J. X., & Forte, A. M. (1997). Radial profile of mantle viscosity: Results from the joint inversion of convection and postglacial rebound observables. *Journal of Geophysical Research*, *102*(B2), 2751–2769. https://doi.org/10.1029/96jb03175

Mitrovica, J. X., & Forte, A. M. (2004). A new inference of mantle viscosity based upon joint inversion of convection and glacial isostatic adjustment data. *Earth and Planetary Science Letters*, *225*(1–2), 177–189. https://doi.org/10.1016/j.epsl.2004.06.005

Moresi, L. N., & Solomatov, V. S. (1995). Numerical investigation of 2D convection with extremely large viscosity variations. *Physics of Fluids*, *7*(9), 2154–2162. https://doi.org/10.1063/1.868465

Panasyuk, S. V., & Hager, B. H. (2000). Inversion for mantle viscosity profiles constrained by dynamic topography and the geoid, and their estimated errors. *Geophysical Journal International*, *143*(3), 821–836. https://doi.org/10.1046/j.0956-540X.2000.01286.x

Ribe, N. M., Stutzmann, E., Ren, Y., & van der Hilst, R. (2007). Buckling instabilities of subducted lithosphere beneath the transition zone. *Earth and Planetary Science Letters*, *254*(1–2), 173–179. https://doi.org/10.1016/j.epsl.2006.11.028

Richards, M. A., & Lenardic, A. (2018). The Cathles parameter (ct): A geodynamic definition of the asthenosphere and implications for the nature of plate tectonics. *Geochemistry, Geophysics, Geosystems*, *19*(12), 4858–4875. https://doi.org/10.1029/2018GC007664

Ritsema, J., Deuss, A., van Heijst, H. J., & Woodhouse, J. H. (2011). S40RTS: A degree-40 shear-velocity model for the mantle from new Rayleigh wave dispersion, teleseismic traveltime and normal-mode splitting function measurements. *Geophysical Journal International*, *184*(3), 1223–1236. https://doi.org/10.1111/j.1365-246X.2010.04884.x

Rudolph, M. L., Lekic, V., & Lithgow-Bertelloni, C. (2015). Viscosity jump in Earth's mid-mantle. *Science*, *350*(6266), 1349–1352. https://doi.org/10.1126/science.aad1929

Simmons, N. A., Myers, S. C., Johannesson, G., & Matzel, E. (2012). LLNL-G3Dv3: Global P wave tomography model for improved regional and teleseismic travel time prediction. *Journal of Geophysical Research*, *117*(B10302), 1–28. https://doi.org/10.1029/2012jb009525

Stegman, D. R., Farrington, R., Capitanio, F. A., & Schellart, W. P. (2010). A regime diagram for subduction styles from 3-D numerical models of free subduction. *Tectonophysics*, *483*(1–2), 29–45. https://doi.org/10.1016/j.tecto.2009.08.041

Tackley, P. J. (1995). Mantle dynamics: Influence of the transition zone. *Reviews of Geophysics*, *33*(S1), 275–282. https://doi.org/10.1029/95RG00291

Tackley, P. J., Stevenson, D. J., Glatzmaier, G. A., & Schubert, G. (1993). Effects of an endothermic phase-transition at 670 km depth in a spherical model of convection in the Earth's mantle. *Nature*, *361*(6414), 699–704. https://doi.org/10.1038/361699a0

Tetzlaff, M., & Schmeling, H. (2000). The influence of olivine metastability on deep subduction of oceanic lithosphere. *Physics of the Earth and Planetary Interiors*, *120*(1–2), 29–38. https://doi.org/10.1016/S0031-9201(00)00139-4

Torii, Y., & Yoshioka, S. (2007). Physical conditions producing slab stagnation: Constraints of the Clapeyron slope, mantle viscosity, trench retreat, and dip angles. *Tectonophysics*, *445*(3–4), 200–209. https://doi.org/10.1016/j.tecto.2007.08.003

van der Meer, D. G., van Hinsbergen, D. J. J., & Spakman, W. (2018). Atlas of the underworld: Slab remnants in the mantle, their sinking history, and a new outlook on lower mantle viscosity. *Tectonophysics*, *723*, 309–448. https://doi.org/10.1016/j.tecto.2017.10.004

Yoshioka, S., & Naganoda, A. (2010). Effects of trench migration on fall of stagnant slabs into the lower mantle. *Physics of the Earth and Planetary Interiors*, *183*(1–2), 321–329. https://doi.org/10.1016/j.pepi.2010.09.002

Zhong, S. J. (2006). Constraints on thermochemical convection of the mantle from plume heat flux, plume excess temperature, and upper mantle temperature. *Journal of Geophysical Research*, *111*(B04409), 1–18. https://doi.org/10.1029/2005jb003972

Zhong, S. J., & Gurnis, M. (1994). Role of plates and temperature-dependent viscosity in phase-change dynamics. *Journal of Geophysical Research*, *99*(B8), 15903–15917. https://doi.org/10.1029/94JB00545

Zhong, S. J., & Gurnis, M. (1995). Mantle convection with plates and mobile, faulted plate margins. *Science*, *267*(5199), 838–843.